Chemical Engineering Journal 451 (2023) 138578

Contents lists available at ScienceDirect

Chemical Engineering Journal

journal homepage: www.elsevier.com/locate/cej

Wearable nanofibrous tactile sensors with fast response and wireless communication

Kangqi Chang, Minhao Guo, Lei Pu, Jiancheng Dong, Le Li, Piming Ma, Yunpeng Huang *, Tianxi Liu *

Key Laboratory of Synthetic and Biological Colloids, Ministry of Education, School of Chemical and Material Engineering, Jiangnan University, Wuxi 214122, China

ARTICLE INFO

Keywords:
Nanofibrous membrane
Tactile sensors
MXene
Human motion monitoring

ABSTRACT

Flexible tactile sensors with high sensitivity and superior stability have captured considerable research interests recently owing to their promising applications in electronic skin and human–machine interfaces. Herein, a hybrid nanofibrous tactile sensor is developed through the co-electrospinning of TPU/PAN/F127 (TPF) nanofibers and subsequent wrapping of mono-layered $Ti_3C_2T_x$ flakes. It is proved that the blending of PAN and F127 can significantly improve the fiber uniformity and the interfacial interaction between the fibrous matrix and MXene, leading to the stable and uniform incorporation of the highly conductive $Ti_3C_2T_x$ flakes. Obtained flexible MXene/TPU/PAN/F127 (MTPF) nanofibrous membrane with interconnected 3D conducting networks manifests a high sensitivity (0.2082 kPa^{-1}), a wide working range (0–160 kPa), rapid response/recovery times (60 ms/120 ms), and long-term durability (8000 cycles) when utilized as an on-skin tactile sensor, which is also assembled into a wearable wireless sensor for the accurate and real-time detection of various human activity signals, evidencing its great potential in high-performance wearable sensory electronics.

1. Introduction

Recently, there has been tremendous interest in the potential applications of flexible pressure sensors in medical diagnostics, human–machine interfaces (HMIs), robotics, and the internet of thing (IoT) [1–6]. Pressure/strain sensors can convert external force into electrical signals or other responsive output signals that are simpler to perceive in order to differentiate and evaluate environmental stimuli [7–11]. Typically, pressure sensors can be divided into four categories depending on the sensing transduction mechanism: piezoresistive sensors, capacitance sensors, piezoelectric sensors, and triboelectric sensors [12–15]. The flexible piezoresistive sensors have received the most attention because of their straightforward design, low cost, and simple manufacturing process [16–19]. The selection and design of conducting materials and flexible substrates (e.g. PDMS [20,21], TPU [22–24], Ecoflex [25,26], etc.) is critical to the overall performance of piezoresistive sensors [27]. A wide class of conducting nanomaterials [28–32], including silver nanowires, carbon black, carbon nanotubes, and graphene have been utilized to construct flexible pressure sensors with a controlled sensing range and high sensitivity. For example, Yang et al. reported a flexible pressure sensor based on polydimethylsiloxane (PDMS)/aluminum-doped zinc oxide (AZO) using traditional micro-nano processing and vacuum coating, the prepared device showed high sensitivity and fast response time [33]. However, it still remains a critical challenge to synchronously obtain a broad sensing range and a high sensitivity.

MXene is a class of early transition metal carbides or nitrides featuring high electrical conductivity and excellent mechanical properties, which is a promising candidate to construct conducting sensing layers in stretchable substrates owing to its tunable surface groups and great processibility in various solvents [28,34–38]. For example, Gao et al. prepared a flexible piezoresistive sensor by spraying MXene on the surface of PDMS with special microstructures, which showed excellent sensitivity (151.4 kPa^{-1}) and cycle stability (10000 cycles) [39]. Impressively, Han et al. reported a hydrophobic composite film using natural elastic P(VDF-TrFE) substrates and multilayer $Ti_3C_2T_x$ by spin-coating, assembled pressure sensor showed an extremely high sensitivity of 817.4 kPa^{-1} in the pressure range of 0.072–0.74 kPa [40]. However, the weak interfacial interaction between MXene and polymeric matrix always results in poor stability of the sensory devices. Hence, surface modification was widely employed to improve the interface between conductive nanomaterials and substrates, which

* Corresponding authors.
E-mail addresses: hypjnu@jiangnan.edu.cn (Y. Huang), txliu@jiangnan.edu.cn (T. Liu).

https://doi.org/10.1016/j.cej.2022.138578
Received 10 June 2022; Received in revised form 24 July 2022; Accepted 8 August 2022
Available online 10 August 2022

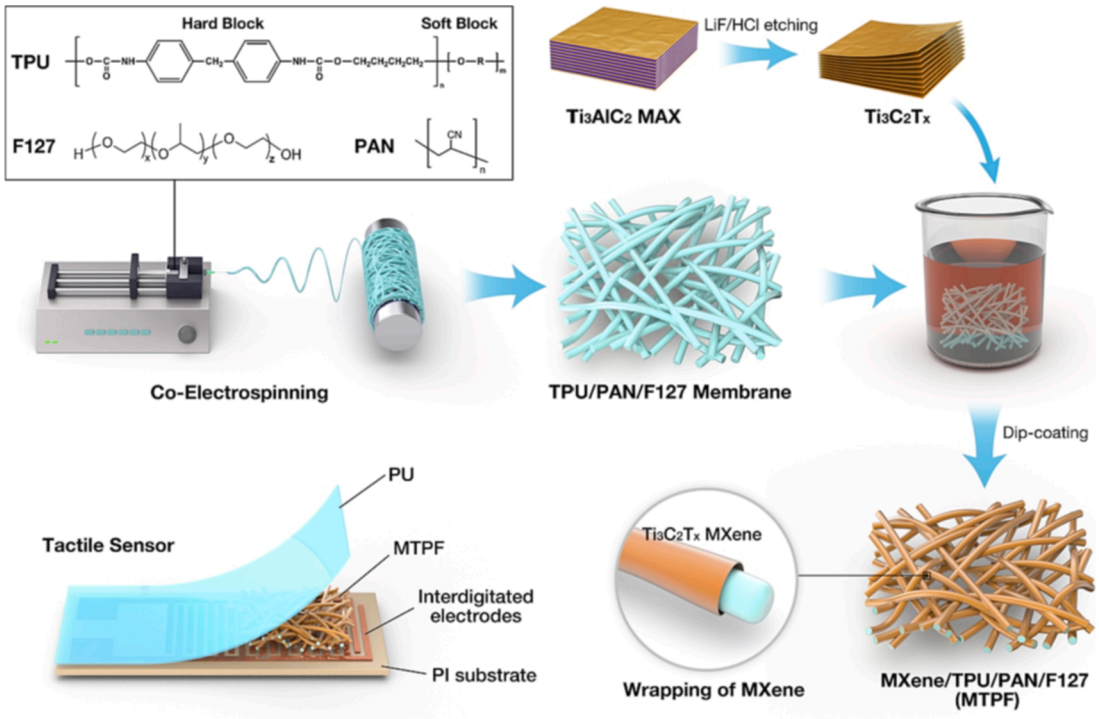

Fig. 1. Schematic illustration for the fabrication of MTPF based tactile sensor.

would unavoidably introduce additional terminals on the MXene flakes, leading to degraded electrical conductivity [41]. Previously, Jing et al. reported the grafting of 4-nitrophenyl groups onto the surface of MXene by solid–liquid reaction, resulting in the significantly increased on/off current ratio of modified MXene (3.56), coupled with a decrease in the conductivity and mobility [42]. Therefore, it is highly preferable to optimize the surface functionality of the flexible substrates rather than modify the surface of MXene.

In this work, highly conductive $Ti_3C_2T_x$ networks were constructed on a TPU-based nanofiber matrix to fabricate a high-performance flexible tactile sensor. Instead of the conventional surface modification on MXene flakes, PAN and F127 as interface-enhancing agents were blended into the TPU matrix by co-electrospinning, thus greatly improving the interaction between $Ti_3C_2T_x$ flakes and the elastomeric substrate. Subsequent tight wrapping of MXene on individual fiber was realized through a low-cost yet efficient dip-coating method, resulting in the successful preparation of conducting MTPF nanofibrous membrane with excellent flexibility and breathability (Fig. 1). Due to the 3D interconnected conducting networks in the hybrid membrane, the MTPF tactile sensor exhibited a wide sensing range (0–160 kPa), a short response time (60 ms), a low detection limit (240 Pa), and excellent durability (8000 cycles). As a result, various human activities from large movements, e.g., finger and elbow bending, to subtle motions of arterial pulse and vocal cord vibrations can be accurately detected by the MTPF tactile sensor. Apart from these, research into large-area sensor arrays and wireless monitoring devices for human physiological signal acquisition further demonstrates the great potential of MTPF in intelligent robots and wearable electronics.

2. Experimental

2.1. Materials

MAX powder (Ti_3AlC_2, 200 mesh) was purchased from Jilin 11 Technology Co., ltd, China. Lithium fluoride (LiF) was obtained from Aladdin Reagent Co., ltd. Concentrated hydrochloric acid (HCl) and analytically pure *N,N*-dimethylformamide (DMF) were supplied by Sinopharm Chemical Reagent Company. Polyacrylonitrile (PAN, M_w = 150,000 g mol^{-1}) and PEO-PPO-PEO triblock copolymer (F127, 12,600 g mol^{-1}) were supplied by Sigma-Aldrich. TPU (1185A) was purchased from BASF Co., ltd. (Shanghai, China). Commercial interdigitated electrodes patterned on polyimide (PI) substrate were purchased from Guangzhou Yuxin Sensor Technology Co., ltd.

2.2. Synthesis of mono-layered $Ti_3C_2T_x$ MXene

A MILD etching method was used to produce $Ti_3C_2T_x$ monolayers [43]. Typically, 2 g LiF was first dissolved in 40 mL 9 M HCl in an acid-proof container, followed by gradual addition of 2 g Ti_3AlC_2 powder, after stirring at 35 °C for 24 h, resulted acidic product was washed with deionized water and centrifuged at 3500 rpm for 10 min. Repeat this procedure until the pH of the supernatant reached 6. Finally, the washed product was exfoliated under ultrasonication in the inert nitrogen flow to obtain a stable mono-layered $Ti_3C_2T_x$ suspension.

2.3. Fabrication of MTPF hybrid membrane

TPU, PAN, and F127 powders at a weight ratio of 8:1:1 were dissolved in 20 mL DMF with a total concentration of 14 wt%. After being stirred at room temperature for 8 h, the three polymers were completely dissolved to obtain the homogeneous spinning solution. For the electrospinning process, the distance from the nozzle to the drum collector was 15 cm and the rotation speed of the collector was 2500 rpm. The pumping speed of the mixed solution was 0.04 mm min^{-1}, the applied positive voltage was 16 kV and the negative voltage was −1 kV. Besides, the humidity was kept at 30 % and the temperature was maintained at around 30 ℃.

The $Ti_3C_2T_x$ flakes were coated on the TPF nanofiber membrane by a straightforward dip-coating process. Typically, the nanofiber membrane (2 cm × 2 cm) was immersed in a $Ti_3C_2T_x$ aqueous dispersion (2 mg mL^{-1}) and sonicated for 1 h in an ice bath, followed by vacuum drying at 60 ℃ for 3 h, thus a uniform MXene layer was incorporated on the TPF nanofibers. For comparison, MXene/TPU and MXene/TPU/PAN fibrous membranes were also prepared by the same method.

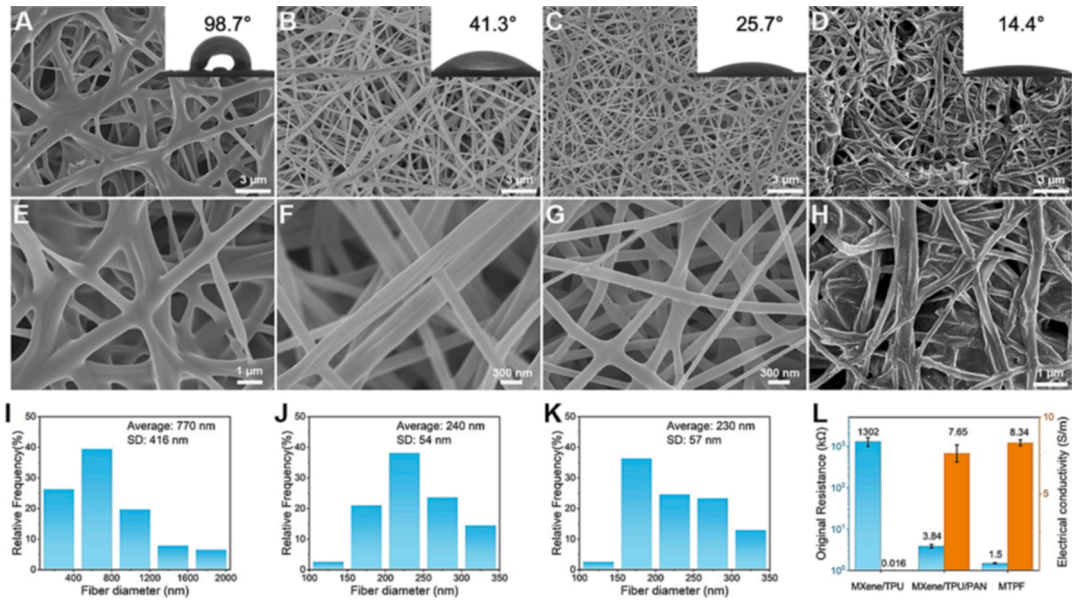

Fig. 2. SEM images of (A, E) TPU, (B, F) TPU/PAN, (C, G) TPF, and (D, H) MTPF nanofibrous membranes, insets are their corresponding water contact angles. Diameter distribution diagrams of (I) TPU, (J) TPU/PAN, and (K) TPF nanofibrous membranes. (L) Histogram showing the resistances and electrical conductivities of the samples.

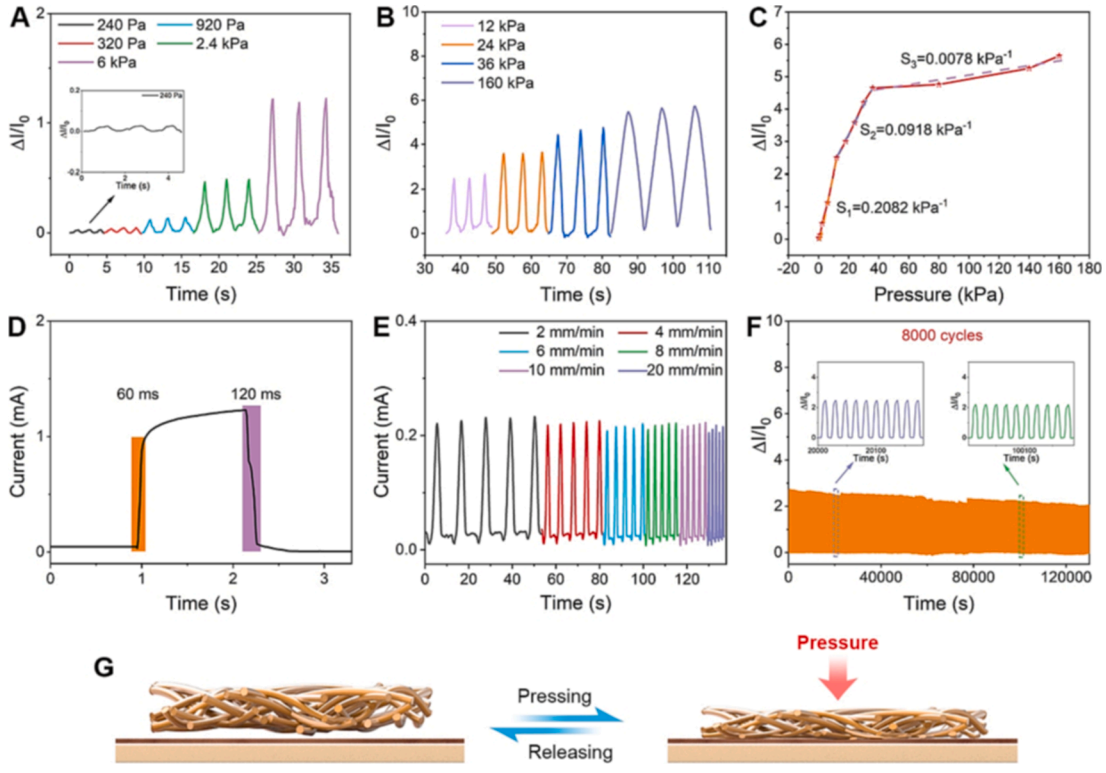

Fig. 3. (A-B) Current responses of the MTPF piezoresistive sensor under various pressures (240 Pa-kPa). (C) Current responses to the external pressures ranging from 0.24 kPa to 160 kPa with a compression rate of 2 mm min^{-1}. (D) The response and recovery times of the pressure sensor. (E) Current responses of the pressure sensor at different compression rates under 12 kPa. (F) Stability test of the sensor under 8000 loading and unloading cycles. (G) Schematic illustration of the sensing mechanism.

2.4. Assembly of the MTPF based tactile sensors

The MTPF tactile sensors were assembled by sandwiching the MTPF nanofiber membrane between elastic translucent PU adhesive tape and an interdigitated electrode. In the device, PU tape was used as the encapsulation layer to protect the pressure sensor from external influences and to stabilize the current signal, and the interdigitated electrode helped to construct a stable conductive path (Fig. 1). The thicknesses of the MTPF nanofiber membrane and PU tape were approximately controlled at 58 μm and 40 μm, respectively.

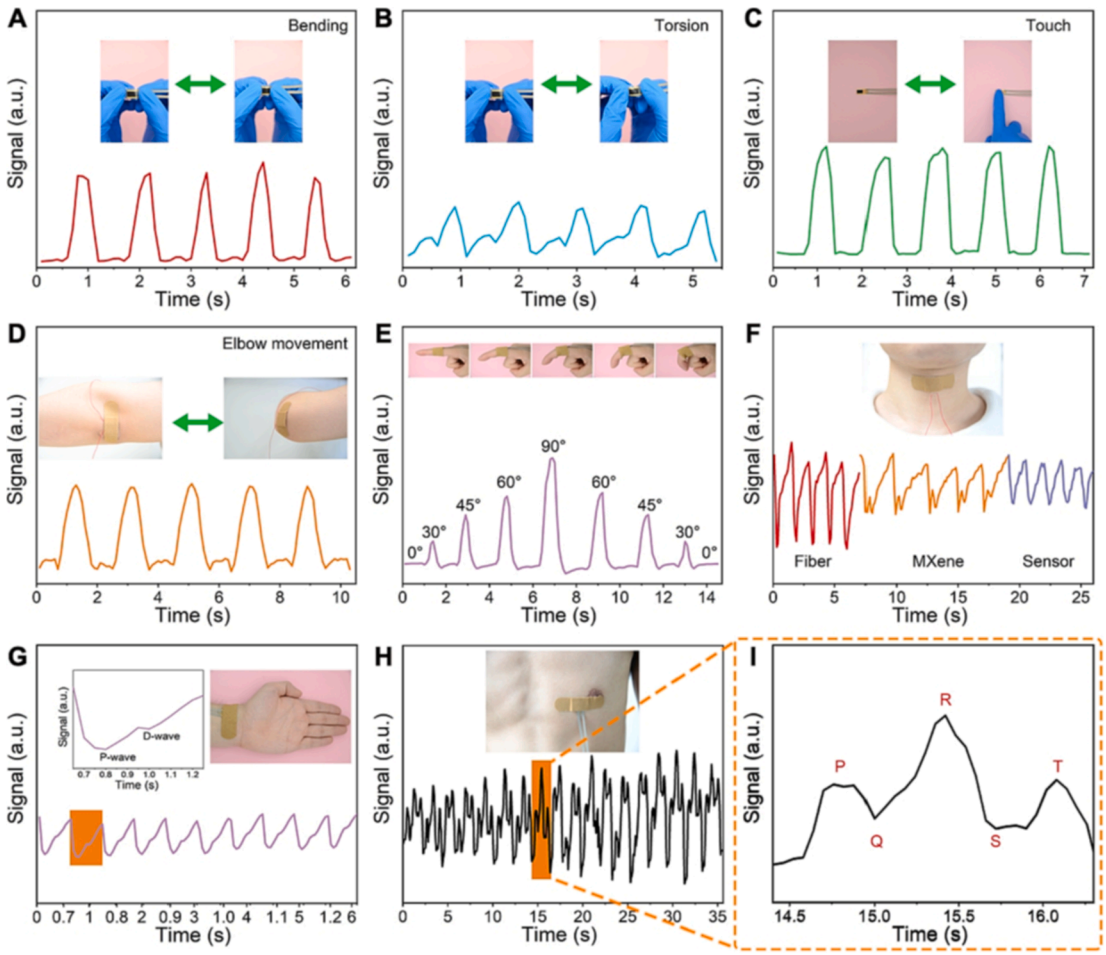

Fig. 4. The cyclic sensing performance of the MTPF tactile sensor constructed on interdigitated electrodes under different loading modes: (A) bending, (B) torsion and (C) touching. Applications of the pressure sensor for human motion detection: (D) Elbow movement, (E) finger bending, (F) vocal cords vibration, (G) wrist pulse, and (H, I) the heart rate curves recorded by the MTPF tactile sensor.

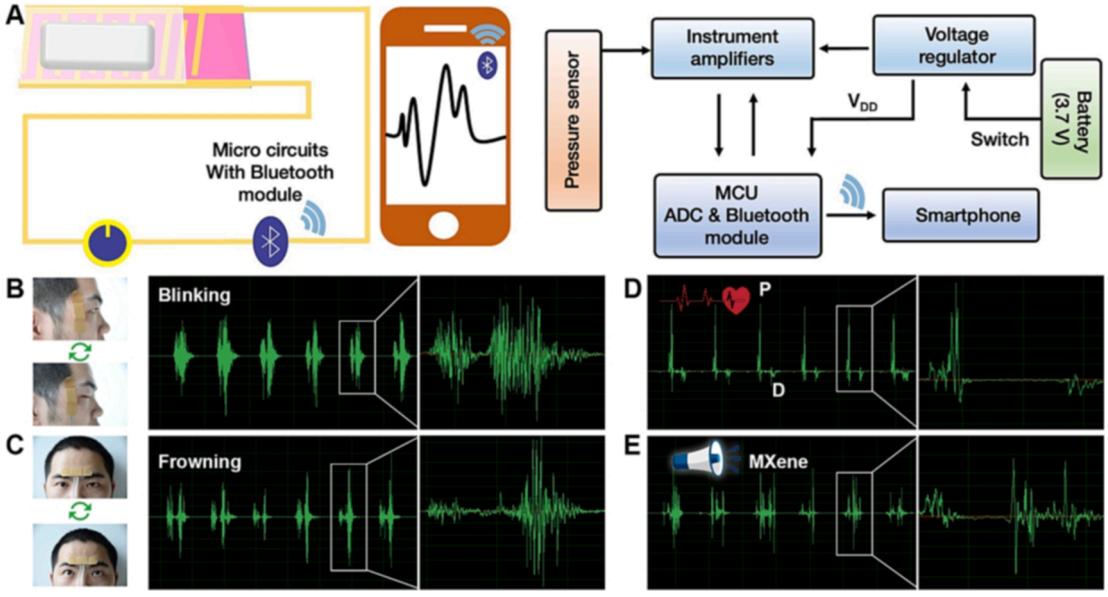

Fig. 5. (A) Construction of the wireless MTPF sensory device, and its applications on the remote monitoring of human motions: (B-C) different facial expressions, (D) pulse detection, and (E) phonation.

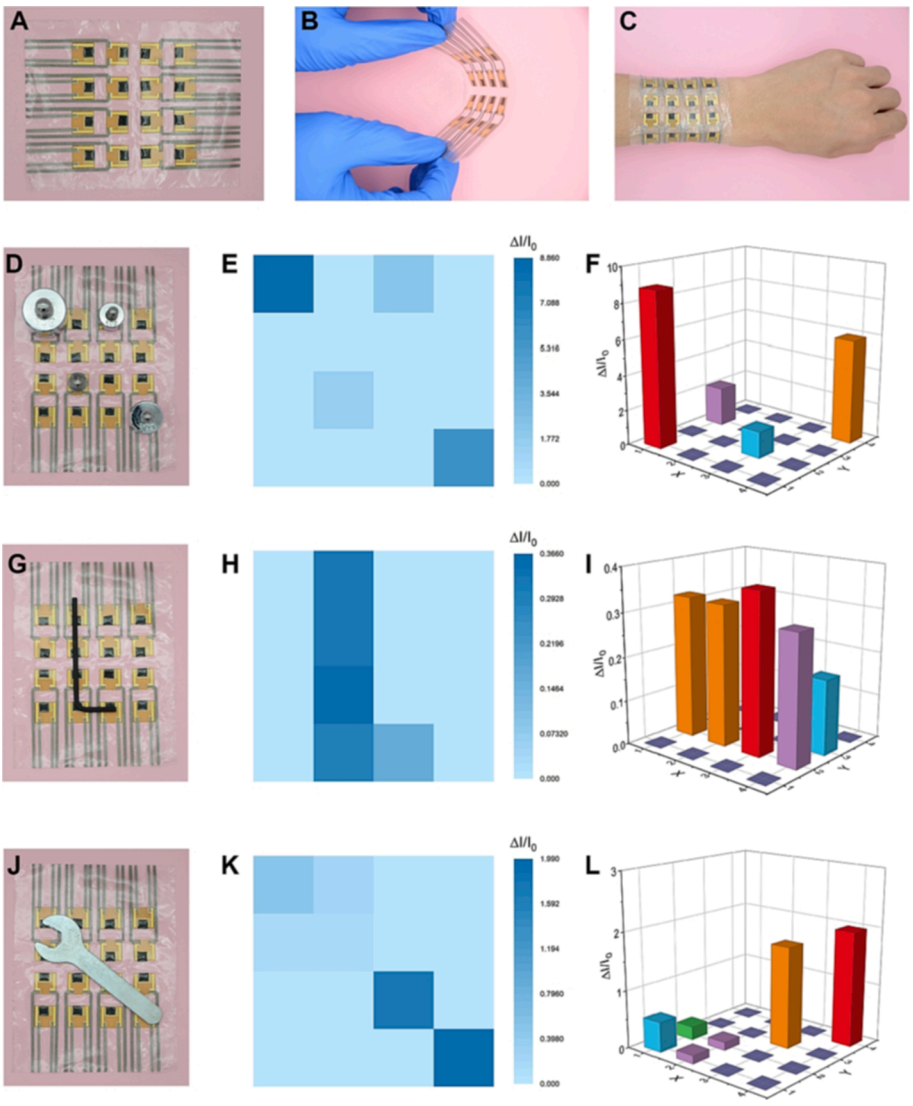

Fig. 6. (A-C) Photographs of the flexible and bendable MTPF based pressure sensor array with 4 × 4 pixels. (D) Photograph of 5 g, 10 g, 15 g, and 20 g weights lying on the sensory device, and (E, F) the corresponding pressure mapping diagrams. (G-L) Photographs and the corresponding pressure mapping diagrams of the assembled sensor loaded with different objects.

2.5. Materials characterization

The synthesized MXene flakes were characterized by atomic force microscopy (AFM, MultiMode 8 system, Bruker). The morphologies of the fibrous membranes were observed by FESEM (HITACHI S-4800). A contact angle goniometer (OCA15EC) was employed to characterize the wettability of the fibrous membranes. X-ray diffraction (XRD) patterns were obtained using a Bruker D2 PHASER X-ray diffractometer with a Cu Ka X-ray source ($\lambda = 1.5406$ Å). An electrochemical workstation (CHI 660E) with a voltage of 0.1 V was used to obtain the *I-t* response curves of the pressure sensors. A digital force gauge (Mark-10 M5) and a motorized force tester (ESM-303) were used to conduct the testing of pressure sensors. A commercial Bluetooth module was used for signal transmission in the wireless wearable sensors. Physiological signals thus could be recorded by a smartphone.

3. Results and discussion

As shown in Fig. S1A, the obtained $Ti_3C_2T_x$ flakes were well dispersed in water, forming a dark green dispersion exhibiting a typical Tyndall effect when irradiated with a laser pointer. Meanwhile, a free-standing film prepared by vacuum filtration of MXene dispersion demonstrated remarkable hydrophilicity with a water contact angle of 25.7° (Fig. S1B). Further AFM characterization revealed that the exfoliated MXene flake had a thickness of ~ 3 nm and a lateral dimension of ~ 1.5 μm (Fig. S1C and S1D), indicating the successful synthesis of mono-layered MXene flakes. Fabricating TPU into a nanofibrous membrane can effectively improve the permeability and mechanical properties of the elastic matrix. In this work, PAN was blended into the spinning solution due to the inferior spinnability of TPU. Additionally, in order to improve the interaction between the flexible substrates and MXene flakes while maintaining the high conductivity of MXene, F127 was also added to TPU/PAN solution to improve the wettability of the polymeric nanofibers, thus enabling the full permeation of the MXene aqueous dispersion into the fiber networks for the complete wrapping.

The fibrous membranes made of TPU, TPU/PAN, and TPU/PAN/F127 (TPF) displayed a homogenous fibrous network with smooth surfaces (Fig. 2A-2C). The mean diameter of electrospun TPU fibers was roughly 770 nm, while the average fiber diameters of TPU/PAN and TPF fibrous membranes decreased to 240 nm and 230 nm, respectively (Fig. 2I-2 K), indicating the blending of PAN and F127 can significantly decrease the fiber diameter of TPU fibers. Besides, the addition of PAN also greatly enhanced the spinnability of TPU, the melted and uneven TPU fibers became clearly and uniformly distributed after only 10 wt%

addition of PAN (Fig. 2B and 2F). The contact angle was also evaluated to assess the wettability of different fibrous membranes. As presented in the insets of Fig. 2A-2C, the water contact angles of TPU, TPU/PAN, and TPF were about 98.7°, 41.3°, and 25.7°, respectively, evidencing the blending of PAN and F127 gradually improved the surface properties of the elastomeric nanofibers. The abundant nitrile groups in PAN and hydroxyl groups in F127 endowed the TPF fibrous membranes with strong affinity with conducting MXene flakes via strong interfacial interaction. Clearly, the white TPF membrane turned to absolute black after dip-coating of MXene (Fig. S2), the MXene flakes were observed intimately and homogeneously wrapped on the fibers without deteriorating the porous structures (Fig. 2D and 2H). The tight interfacial interaction is owing to the strong hydrogen bonding between the hydroxyl groups on TPF fibers and the functional groups (-O, –OH, -F) on MXene flakes. Additionally, the elemental mapping demonstrated that the F and Ti elements of MXene were uniformly distributed on the MTPF nanofiber membrane (Fig. S3), verifying that MXene was successfully deposited on the nanofibrous matrix.

The original resistances and electrical conductivities of the three fiber membranes were compared in Fig. 2L, MTPF exhibited the lowest original resistance and the highest electrical conductivity due to the homogeneous distribution and the tight wrapping of MXene on each TPF fiber, which stemmed from the superior affinity of the ternary nonwoven membrane for MXene flakes. By contrast, MXene/TPU showed negligible conductivity due to the uneven coverage of $Ti_3C_2T_x$ on the less-functionalized fiber surfaces (Fig. S4A). Because of the largely improved interfacial interaction between MXene and TPU/PAN nanofibers, MXene/TPU/PAN membrane manifested significantly enhanced electrical conductivity attributing to the better incorporation of MXene flakes (Fig. S4B). XRD measurements were carried out to study the crystal structures of the fibrous samples. As presented in Fig. S5, the vacuum-filtrated MXene membrane showed a sharp (0 0 2) diffraction peak at $2\theta = 7.6°$ [44,45], this prominent peak of MXene was detected in the MTPF nanofibrous membrane, which shifted from 7.6° to 6.64° ascribing to the enlarged interlayer spacing of MXene layers during incorporation with nanofibers.

The piezoresistive sensing performance of fabricated MTPF fibrous membrane was systematically evaluated. Fig. 3A and 3B show the static current responses of the MTPF sensor at nine different pressure levels. It implies that the detected current signals were repetitive and stable at three cycles, indicating the excellent stability of the prepared nanofibrous sensor. It is also notable that the pressure sensor was capable of discriminating different degrees of forces from 240 Pa to 160 kPa, implying the low detection limit, broad sensing range, and excellent ability for detecting complex pressures. The relative current change of the MTPF sensor under pressures ranging from 0 to 160 kPa is shown in Fig. 3C, suggesting the sensor prepared using the MTPF membrane can work over a wide range. The slope of the current response curve at various pressures can be used to calculate the sensitivity according to the following Equation (1),

$$S = \frac{\Delta I}{I_0 \Delta P} = \frac{(I - I_0)}{I_0 \Delta P} \quad (1)$$

where P is the value of the applied pressure, I denotes the current flowing through the sensor system under pressure, and I_0 defines the current when no pressure was applied. Notably, the sensitivity of the MTPF sensor was as high as 0.2082 kPa^{-1} in a low-pressure range (below 12 kPa), which decreases to 0.0918 kPa^{-1} in the comparatively high-pressure range (12–36 kPa), finally, the sensitivity stabilized at 0.0078 kPa^{-1} (Fig. 3C). The decreasing trend in sensitivity with increased applied pressure is mainly correlated to the sensor's internal structural change caused by the piezoresistive sensing mechanism. Because the MTPF membrane has a highly interconnected 3D conducting structure, which may manifests a staged deformation phenomenon during the compressing process. When a tiny force was applied to the pressure sensor, the electrical contact area between the MTPF fibers increased significantly to form conductive networks, resulting in the large S value of the pressure sensor. When the external load increased to higher pressure beyond 12 kPa, the conductive networks during compression increased slower to yield a lower sensitivity of 0.092 kPa^{-1}. When the MTPF-based pressure sensor was subjected to a larger external force (i.e., >36 kPa), the conductive pathways generated by contact of fibers became saturated, thus the rise in the current value ($\triangle I$) was limited, resulting in a greatly decreased S value in the high-pressure region.

After that, the response and recovery times were measured to evaluate the applicability of MTPF for sensory electronics. As shown in Fig. 3D, the response and recovery times of the pressure sensor are 60 ms and 120 ms, respectively, indicating the quick response and fast establishment of conducting paths in the conducting nanofibrous membrane, endowing itself with great potential in the real-time monitoring of human physiological signals. Additionally, Fig. 3E also illustrates the cyclic pressure sensing performance of the MTPF-based pressure sensor when subjected to a pressure with different compression rates. Stable sensing behavior can be observed at various compression rates from 2 mm min^{-1} to 20 mm min^{-1}, exhibiting the typical rate-independent sensing performance, which is conducive to the stable detection of complicated human motions at different speeds. The capacity of the sensors to resist cyclic loading/unloading pressure without losing electrical and mechanical functionality is defined as cyclic stability. As illustrated in Fig. 3F, it is discovered that the $\Delta I/I_0$ remained relatively stable with a retention of 80 % after 8000 repeated loading/unloading cycles at 12 kPa. The minor decrease of the relative current was mostly induced by the unavoidable destruction of conducting paths under large strains. The excellent sensing performance suggests the potential applications of the MTPF in wearable electronic devices. The sensing performance was further compared with those of the previously published piezoresistive pressure sensors (Table S1), it is obvious that our designed nanofibrous tactile sensor manifests competitive sensitivity, sensing range, and response/recovery times. The structural evolution of the MTPF-based pressure sensor under external pressure is schematically shown in Fig. 3G. The overall resistance of the sensor is primarily comprised of the MTPF resistance and the contact resistance between the MTPF and the interdigitated electrode. When the membrane is subjected to external force, the contact areas between the MTPF fibers, as well as the membrane and the interdigitated electrode significantly expand even under subtle pressure, resulting in the creation of countless new conducting networks and a significant decrease in the overall resistance. This synergistic effect is responsible for the sharp increase of current and the improvement of sensitivity. As the external pressure further increases, the MTPF networks tend to be saturated due to the densification of the MTPF fibrous membrane at high pressure, resulting in the insignificant change in both the MTPF resistance and the contact resistance.

Based on the above characterizations of piezoresistive sensing performance, further assessment of human motion detection was performed. As demonstrated in Fig. 4, the pressure sensor was capable of detecting various forms of stresses including bending and torsion. Reproducible and constant current responses were obtained in Fig. 4A-4C when the sensor was applied to cyclic bending, torsion, and touching, indicating its reliable sensing capabilities under multiple loading modes and potential in wearable electronics. As can be observed in Fig. 4D, the flexible motion sensor was attached to the elbow to monitor the joint bending by repeatedly swinging the arm, acquired current responses were stable and reproducible during cyclic movements. Additionally, Fig. 4E shows that the MTPF sensor can also be used to discriminate different gesture signals. The collected signal rose as the finger bent at different angles, exhibiting the excellent sensibility and flexibility of the MTPF sensor. What's more, the flexible sensory device was further connected to the throat with adhesive PU tape to simultaneously monitor the vocal cord's vibrations. Apparently, there was a significant

difference in the current signals when the volunteer uttered the words "Fiber", "MXene", and "Sensor" (Fig. 4F), and reproducible waveforms can be generated when the words were repeatedly spoken five times, verifying the prominent ability of the MTPF strain sensor for subtle motion detection. The pressure sensor was attached to the radial artery of a 27-year-old male to further evaluate its accuracy for physiological signals. The distinctive peaks ascribed to the artery pulse were collected and identified in Fig. 4G, where P-wave and D-wave corresponding to percussion wave and diastolic pressure were clearly observed. Finally, the sensor was able to detect heartbeat signals by measuring the contraction and relaxation of the blood artery. As shown in Fig. 4H and 4I, the distinctive peaks ascribed to the P-wave, QRS-wave, and D-wave of heartbeat were collected and clearly identified, demonstrating the potential application of the MTPF sensor in health monitoring and illness surveillance.

To further explore the practical applications of the MTPF-based tactile sensor for human physical signal monitoring, a wireless MTPF sensory device was constructed with the diagram shown in Fig. 5A. Briefly, the MTPF sensor was coupled with a customized Bluetooth module, which can receive and transfer motion signals to the smartphone for recording and displaying. For the detection of subtle facial expressions including blinking and frowning, the recorded signals showed fast response and repeatability, the slightly fluctuated signal intensity of the same facial motion was caused by the delay of Bluetooth transmission (Fig. 5B and 5C). The two peaks in each wave pattern corresponded to the muscle contraction and the muscle relaxation, respectively, and the gap between the two peaks was proportional to the motion duration. Besides, pulse signals with varying rates and waveforms are often essential indications of human physiological variables such as arterial pressure, blood vessel elasticity, and so forth. Fig. 5D depicts the sphygmogram signals collected from the wireless sensor were as stable and repeatable as those obtained from the electrochemical workstation. The characteristic P-wave and D-wave also can be detected by this wireless sensor. As a result, pulse monitoring through the assembled MTPF wireless wearable sensor can provide a straightforward strategy for health management. Meanwhile, this wireless sensor also can be used for throat vibration recognition. As presented in Fig. 5E, the speaking process of the word "MXene" was accurately recorded. The above results imply that the wearable pressure sensor based on the MTPF membrane is capable of remotely monitoring personal health status in real time.

Because of the excellent flexibility and sensitivity of the MTPF piezoresistive sensor, multiple pressure sensors can be assembled on the flexible substrates for tactile force mapping. As demonstrated in Fig. 6, a large-area pressure sensor was built to test the efficacy of large-area pressure sensing for future applications such as electronic skin by fabricating a 4 × 4 sensor array using 16 MTPF (Fig. 6A). The sensory device can be bent and attached to the human skin to record external force due to the sensor's extraordinary flexibility (Fig. 6B and 6C). Importantly, when objects with different weights were loaded on the sensor array, detected pressure mapping can precisely represent their unique position and pressure (Fig. 6D-F). Meanwhile, the pressure mapping also can be utilized to determine the exact shape and position of an Allen wrench and an open-end wrench (Fig. 6G-6L). In short, the MTPF-based tactile sensor can be used in a variety of sophisticated and flexible E-skin devices for next-generation wearable electronics.

4. Conclusions

In summary, we propose here an efficient strategy to enhance the interfacial interaction between MXene and polymer nanofibrous substrate to construct a high-performance wearable tactile sensor by improving the composition of TPU nanofibers. As a result, stable MTPF conductive networks were achieved based on the tight wrapping of mono-layered $Ti_3C_2T_x$ flakes on the electrospun TPU/PAN/F127 nanofibers. Benefiting from the excellent flexibility and the three-dimensional porous structures, the obtained functional membrane manifested remarkable piezoresistive sensing performance in terms of high sensitivity (0.2082 kPa^{-1}), wide working range (0–160 kPa), rapid response and recovery times (60/120 ms), and long-term durability (8000 cycles). Meanwhile, the pressure sensors were also integrated into a large-area sensory array for pressure mapping, as well as a wireless tactile sensor for the real-time monitoring of various human movements. Therefore, this research provides a simple and efficient approach to the development of advanced wearable sensory electronics.

Declaration of Competing Interest

The authors declare that they have no known competing financial interests or personal relationships that could have appeared to influence the work reported in this paper.

Data availability

The authors do not have permission to share data.

Acknowledgments

This work is financially supported by the National Natural Science Foundation of China (21875033), the Shanghai Scientific and Technological Innovation Project (18JC1410600), the Program of the Shanghai Academic Research Leader (17XD1400100), and the State Key Laboratory for Modification of Chemical Fibers and Polymer Materials, Donghua University.

Appendix A. Supplementary data

Supplementary data to this article can be found online at https://doi.org/10.1016/j.cej.2022.138578.

References

[1] X. Cao, J. Zhang, S. Chen, R.J. Varley, K. Pan, 1D/2D nanomaterials synergistic, compressible, and response rapidly 3D graphene aerogel for piezoresistive sensor, Adv. Funct. Mater. 30 (35) (2020) 2003618, https://doi.org/10.1002/adfm.202003618.
[2] J. Dong, D. Wang, Y. Peng, C. Zhang, F. Lai, G. He, P. Ma, W. Dong, Y. Huang, I. P. Parkin, T. Liu, Ultra-stretchable and superhydrophobic textile-based bioelectrodes for robust self-cleaning and personal health monitoring, Nano Energy 97 (2022), 107160, https://doi.org/10.1016/j.nanoen.2022.107160.
[3] B. An, Y. Ma, W. Li, M. Su, F. Li, Y. Song, Three-dimensional multi-recognition flexible wearable sensor via graphene aerogel printing, Chem. Commun. 52 (73) (2016) 10948–10951, https://doi.org/10.1039/C6CC05910D.
[4] M. Naguib, O. Mashtalir, J. Carle, V. Presser, J. Lu, L. Hultman, Y. Gogotsi, M. W. Barsoum, Two-dimensional transition metal carbides, ACS Nano 6 (2) (2012) 1322–1331, https://doi.org/10.1021/nn204153h.
[5] Y. Wang, M. Zhu, X. Wei, J. Yu, Z. Li, B. Ding, A dual-mode electronic skin textile for pressure and temperature sensing, Chem. Eng. J. 425 (2021), 130599, https://doi.org/10.1016/j.cej.2021.130599.
[6] M. Zhu, M. Lou, J. Yu, Z. Li, B. Ding, Energy autonomous hybrid electronic skin with multi-modal sensing capabilities, Nano Energy 78 (2020), 105208, https://doi.org/10.1016/j.nanoen.2020.105208.
[7] L. Pu, Y. Liu, L. Li, C. Zhang, P. Ma, W. Dong, Y. Huang, T. Liu, Polyimide nanofiber-reinforced $Ti_3C_2T_x$ aerogel with "lamella-pillar" microporosity for high-performance piezoresistive strain sensing and electromagnetic wave absorption, ACS Appl. Mater. Interfaces 13 (39) (2021) 47134–47146, https://doi.org/10.1021/acsami.1c13863.
[8] C. Fan, D. Wang, J. Huang, H. Ke, Q. Wei, A highly sensitive epidermal sensor based on triple-bonded hydrogels for strain/pressure sensing, Compos. Commun. 28 (2021), 100951, https://doi.org/10.1016/j.coco.2021.100951.
[9] L. Liu, Y. Huang, F. Li, Y. Ma, W. Li, M. Su, X. Qian, W. Ren, K. Tang, Y. Song, Spider-web inspired multi-resolution graphene tactile sensor, Chem. Commun. 54 (38) (2018) 4810–4813, https://doi.org/10.1039/C8CC02339E.
[10] L. Pu, H. Ma, J. Dong, C. Zhang, F. Lai, G. He, P. Ma, W. Dong, Y. Huang, T. Liu, Xylem-inspired polyimide/MXene aerogels with radial lamellar architectures for highly sensitive strain detection and efficient solar steam generation, Nano Lett. (2022), https://doi.org/10.1021/acs.nanolett.2c01486.
[11] M. Zhu, J. Li, J. Yu, Z. Li, B. Ding, Superstable and intrinsically self-healing fibrous membrane with bionic confined protective structure for breathable electronic skin, Angew. Chem., Int. Ed. 61 (22) (2022) e202200226.

[12] P. Zhang, Y. Chen, Z.H. Guo, W. Guo, X. Pu, Z.L. Wang, Stretchable, transparent, and thermally stable triboelectric nanogenerators based on solvent-free Ion-conducting elastomer electrodes, Adv. Funct. Mater. 30 (15) (2020) 1909252, https://doi.org/10.1002/adfm.201909252.
[13] Z. Han, Z. Cheng, Y. Chen, B. Li, Z. Liang, H. Li, Y. Ma, X. Feng, Fabrication of highly pressure-sensitive, hydrophobic, and flexible 3D carbon nanofiber networks by electrospinning for human physiological signal monitoring, Nanoscale 11 (13) (2019) 5942–5950, https://doi.org/10.1039/C8NR08341J.
[14] L. Yuan, W. Fan, X. Yang, S. Ge, C. Xia, S.Y. Foong, R.K. Liew, S. Wang, Q. Van Le, S.S. Lam, Piezoelectric PAN/$BaTiO_3$ nanofiber membranes sensor for structural health monitoring of real-time damage detection in composite, Compos. Commun. 25 (2021), 100680, https://doi.org/10.1016/j.coco.2021.100680.
[15] M. Zhu, Y. Wang, M. Lou, J. Yu, Z. Li, B. Ding, Bioinspired transparent and antibacterial electronic skin for sensitive tactile sensing, Nano Energy 81 (2021), 105669, https://doi.org/10.1016/j.nanoen.2020.105669.
[16] M. Cao, J. Su, S. Fan, H. Qiu, D. Su, L. Li, Wearable piezoresistive pressure sensors based on 3D graphene, Chem. Eng. J. 406 (2021), 126777, https://doi.org/10.1016/j.cej.2020.126777.
[17] Y. Zheng, R. Yin, Y. Zhao, H. Liu, D. Zhang, X. Shi, B. Zhang, C. Liu, C. Shen, Conductive MXene/cotton fabric based pressure sensor with both high sensitivity and wide sensing range for human motion detection and E-skin, Chem. Eng. J. 420 (2021), 127720, https://doi.org/10.1016/j.cej.2020.127720.
[18] Q. Zheng, J.-H. Lee, X. Shen, X. Chen, J.-K. Kim, Graphene-based wearable piezoresistive physical sensors, Mater. Today 36 (2020) 158–179, https://doi.org/10.1016/j.mattod.2019.12.004.
[19] R. Tong, L. Cai, G. Chen, J. Tian, M. He, Rapid preparation of highly transparent piezoresistive balls for optoelectronic devices, Chem. Commun. 56 (18) (2020) 2771–2774, https://doi.org/10.1039/C9CC08840G.
[20] B. Nie, X. Li, J. Shao, X. Li, H. Tian, D. Wang, Q. Zhang, B. Lu, Flexible and transparent strain sensors with embedded multiwalled carbon nanotubes meshes, ACS Appl. Mater. Interfaces 9 (46) (2017) 40681–40689, https://doi.org/10.1021/acsami.7b12987.
[21] F. Zhang, S. Wu, S. Peng, Z. Sha, C.H. Wang, Synergism of binary carbon nanofibres and graphene nanoplates in improving sensitivity and stability of stretchable strain sensors, Compos. Sci. Technol. 172 (2019) 7–16, https://doi.org/10.1016/j.compscitech.2018.12.031.
[22] Y. Huang, X. You, X. Fan, C.P. Wong, P. Guo, N. Zhao, Near-field electrospinning enabled highly sensitive and anisotropic strain sensors, Adv. Mater. Technol. 5 (11) (2020) 2000550, https://doi.org/10.1002/admt.202000550.
[23] X. Wang, H. Sun, X. Yue, Y. Yu, G. Zheng, K. Dai, C. Liu, C. Shen, A highly stretchable carbon nanotubes/thermoplastic polyurethane fiber-shaped strain sensor with porous structure for human motion monitoring, Compos. Sci. Technol. 168 (2018) 126–132, https://doi.org/10.1016/j.compscitech.2018.09.006.
[24] Y. Wang, J. Hao, Z. Huang, G. Zheng, K. Dai, C. Liu, C. Shen, Flexible electrically resistive-type strain sensors based on reduced graphene oxide-decorated electrospun polymer fibrous mats for human motion monitoring, Carbon 126 (2018) 360–371, https://doi.org/10.1016/j.carbon.2017.10.034.
[25] Z. Tang, S. Jia, F. Wang, C. Bian, Y. Chen, Y. Wang, B. Li, Highly stretchable core–sheath fibers via wet-spinning for wearable strain sensors, ACS Appl. Mater. Interfaces 10 (7) (2018) 6624–6635, https://doi.org/10.1021/acsami.7b18677.
[26] M. Xu, J. Qi, F. Li, Y. Zhang, Highly stretchable strain sensors with reduced graphene oxide sensing liquids for wearable electronics, Nanoscale 10 (11) (2018) 5264–5271, https://doi.org/10.1039/C7NR09022F.
[27] L. Gao, K. Cao, X. Hu, R. Xiao, B. Gan, W. Wang, Y. Lu, Nano electromechanical approach for flexible piezoresistive sensor, Appl. Mater. Today 18 (2020), 100475, https://doi.org/10.1016/j.apmt.2019.100475.
[28] Z. Yang, H. Li, S. Zhang, X. Lai, X. Zeng, Superhydrophobic MXene@carboxylated carbon nanotubes/carboxymethyl chitosan aerogel for piezoresistive pressure sensor, Chem. Eng. J. 425 (2021), 130462, https://doi.org/10.1016/j.cej.2021.130462.
[29] X. Shuai, P. Zhu, W. Zeng, Y. Hu, X. Liang, Y. Zhang, R. Sun, C.-P. Wong, Highly sensitive flexible pressure sensor based on silver nanowires-embedded polydimethylsiloxane electrode with microarray structure, ACS Appl. Mater. Interfaces 9 (31) (2017) 26314–26324, https://doi.org/10.1021/acsami.7b05753.
[30] X. Sun, S. He, Z. Qin, J. Li, F. Yao, Fast self-healing zwitterion nanocomposite hydrogel for underwater sensing, Compos. Commun. 26 (2021), 100784, https://doi.org/10.1016/j.coco.2021.100784.
[31] K. Chang, L. Li, C. Zhang, P. Ma, W. Dong, Y. Huang, T. Liu, Compressible and robust PANI sponge anchored with erected MXene flakes for human motion detection, Compos. A 151 (2021), 106671, https://doi.org/10.1016/j.compositesa.2021.106671.
[32] J. Dong, L. Li, C. Zhang, P. Ma, W. Dong, Y. Huang, T. Liu, Ultra-highly stretchable and anisotropic SEBS/F127 fiber films equipped with adaptive deformable carbon nanotube layer for dual-mode strain sensing, J. Mater. Chem. A 9 (34) (2021) 18294, https://doi.org/10.1039/D1TA04563F.
[33] K. He, Y. Hou, C. Yi, N. Li, F. Sui, B. Yang, G. Gu, W. Li, Z. Wang, Y. Li, G. Tao, L. Wei, C. Yang, M. Chen, High-performance zero-standby-power-consumption-under-bending pressure sensors for artificial reflex arc, Nano Energy 73 (2020), 104743, https://doi.org/10.1016/j.nanoen.2020.104743.
[34] Y. Wei, P. Zhang, R.A. Soomro, Q. Zhu, B. Xu, Advances in the synthesis of 2D MXenes, Adv. Mater. 33 (39) (2021) 2103148, https://doi.org/10.1002/adma.202103148.
[35] H. Liu, X. Chen, Y. Zheng, D. Zhang, Y. Zhao, C. Wang, C. Pan, C. Liu, C. Shen, Lightweight, superelastic, and hydrophobic polyimide nanofiber /MXene composite aerogel for wearable piezoresistive sensor and oil/water separation applications, Adv. Funct. Mater. 31 (13) (2021) 2008006, https://doi.org/10.1002/adfm.202008006.
[36] J. Yan, Y. Ma, G. Jia, S. Zhao, Y. Yue, F. Cheng, C. Zhang, M. Cao, Y. Xiong, P. Shen, Y. Gao, Bionic MXene based hybrid film design for an ultrasensitive piezoresistive pressure sensor, Chem. Eng. J. 431 (2022) 133458.
[37] R. Li, X. Tian, M. Wei, A. Dong, X. Pan, Y. He, X. Song, H. Li, Flexible pressure sensor based on cigarette filter and highly conductive MXene sheets, Compos. Commun. 27 (2021), 100889, https://doi.org/10.1016/j.coco.2021.100889.
[38] X. Wang, J. Lu, S. Lu, B. Li, L. Zhang, C. Ma, K. Ma, L. Lin, X. Jiang, B. Yang, Health monitoring of repaired composite structure using MXene sensor, Compos. Commun. 27 (2021), 100850, https://doi.org/10.1016/j.coco.2021.100850.
[39] Y. Cheng, Y. Ma, L. Li, M. Zhu, Y. Yue, W. Liu, L. Wang, S. Jia, C. Li, T. Qi, J. Wang, Y. Gao, Bioinspired microspines for a high-performance spray $Ti_3C_2T_x$ MXene-based piezoresistive sensor, ACS Nano 14 (2) (2020) 2145–2155, https://doi.org/10.1021/acsnano.9b08952.
[40] L. Li, X. Fu, S. Chen, S. Uzun, A.S. Levitt, C.E. Shuck, W. Han, Y. Gogotsi, Hydrophobic and stable MXene–polymer pressure sensors for wearable electronics, ACS Appl. Mater. Interfaces 12 (13) (2020) 15362–15369, https://doi.org/10.1021/acsami.0c00255.
[41] J.L. Hart, K. Hantanasirisakul, A.C. Lang, B. Anasori, D. Pinto, Y. Pivak, J.T. van Omme, S.J. May, Y. Gogotsi, M.L. Taheri, Control of MXenes' electronic properties through termination and intercalation, Nat. Commun. 10 (1) (2019) 522, https://doi.org/10.1038/s41467-018-08169-8.
[42] H. Jing, H. Yeo, B. Lyu, J. Ryou, S. Choi, J.-H. Park, B.H. Lee, Y.-H. Kim, S. Lee, Modulation of the electronic properties of MXene ($Ti_3C_2T_x$) via surface-covalent functionalization with diazonium, ACS Nano 15 (1) (2021) 1388–1396, https://doi.org/10.1021/acsnano.0c08664.
[43] M. Alhabeb, K. Maleski, B. Anasori, P. Lelyukh, L. Clark, S. Sin, Y. Gogotsi, Guidelines for synthesis and processing of two-dimensional titanium carbide ($Ti_3C_2T_x$ MXene), Chem. Mater. 29 (18) (2017) 7633–7644, https://doi.org/10.1021/acs.chemmater.7b02847.
[44] J. Wang, Y. Liu, Z. Cheng, Z. Xie, L. Yin, W. Wang, Y. Song, H. Zhang, Y. Wang, Z. Fan, Highly conductive MXene film actuator based on moisture gradients, Angew. Chem. Int. Ed. 59 (33) (2020) 14029–14033.
[45] L. Wang, M. Zhang, B. Yang, J. Tan, X. Ding, Highly compressible, thermally stable, light-weight, and robust aramid nanofibers/Ti_3AlC_2 MXene composite aerogel for sensitive pressure sensor, ACS Nano 14 (8) (2020) 10633–10647, https://doi.org/10.1021/acsnano.0c04888.